

University of Wollongong

Research Online

Australian Institute for Innovative Materials -
Papers

Australian Institute for Innovative Materials

1-1-2017

CoS Quantum Dot Nanoclusters for High-Energy Potassium-Ion Batteries

Hong Gao

University of Wollongong, hg173@uowmail.edu.au

Tengfei Zhou

University of Wollongong, tz765@uowmail.edu.au

Yang Zheng

University of Wollongong, yz966@uowmail.edu.au

Qing Zhang

University of Wollongong, qz964@uowmail.edu.au

Yuqing Liu

University of Wollongong, yl037@uowmail.edu.au

See next page for additional authors

Follow this and additional works at: <https://ro.uow.edu.au/aiimpapers>



Part of the [Engineering Commons](#), and the [Physical Sciences and Mathematics Commons](#)

Research Online is the open access institutional repository for the University of Wollongong. For further information contact the UOW Library: research-pubs@uow.edu.au

CoS Quantum Dot Nanoclusters for High-Energy Potassium-Ion Batteries

Abstract

Potassium-ion batteries (PIBs) are a promising alternative to lithium-ion batteries because potassium is an abundant natural resource. To date, PIBs are in the early stages of exploration and only a few anode materials have been investigated. This study reports a cobalt sulfide and graphene (CoS@G) composite as anode electrode for PIBs for the first time. The composite features interconnect quantum dots of CoS nanoclusters uniformly anchored on graphene nanosheets. The coexistence of CoS quantum dot nanoclusters and graphene nanosheets endows the composite with large surface area, highly conductive network, robust structural stability, and excellent electrochemical energy storage performance. An unprecedented capacity of 310.8 mA h g⁻¹ at 500 mA g⁻¹ is obtained after 100 cycles, with a rate capability better than an equivalent sodium-ion batteries (SIBs). This work provides the evidence that PIBs can be a promising alternative to SIBs, especially at high charge-discharge rates. The development of the CoS@G anode material also provides the basis of expanding the library of suitable anode materials for PIBs.

Disciplines

Engineering | Physical Sciences and Mathematics

Publication Details

Gao, H., Zhou, T., Zheng, Y., Zhang, Q., Liu, Y., Chen, J., Liu, H. & Guo, Z. (2017). CoS Quantum Dot Nanoclusters for High-Energy Potassium-Ion Batteries. *Advanced Functional Materials*, 27 (43), 1702634-1-1702634-9.

Authors

Hong Gao, Tengfei Zhou, Yang Zheng, Qing Zhang, Yuqing Liu, Jun Chen, Hua-Kun Liu, and Zaiping Guo

CoS Quantum Dots-Nanoclusters for High-Energy Potassium Ion Battery

Hong Gao, Tengfei Zhou, Yang Zheng, Qing Zhang, Yuqing Liu, Jun Chen,^{*} Huakun Liu, and Zaiping Guo^{*}

Potassium ion batteries (PIBs) are a promising alternative to lithium-ion batteries (LIBs), because potassium is an abundant natural resource. To date, PIBs are in the early stages of exploration and a few anode materials have been investigated. Here, we report a cobalt sulfide and graphene (CoS@G) composite as anode electrode for PIBs for the first time. The composite features interconnected quantum dots of CoS nanoclusters uniformly anchored on graphene nanosheets. The coexistence of CoS quantum dots-nanoclusters and graphene nanosheets endow the composite with large surface area, highly conductive network, robust structural stability and excellent electrochemical energy storage performance. An unprecedented capacity of 310.8 mA h g⁻¹ at 500 mA g⁻¹ is obtained after 100 cycles, with a rate capability better than an equivalent sodium ion batteries (SIBs). This work provides the evidence that PIBs could be a promising alternative to SIBs, especially at high charge-discharge rates. The development of the CoS@G anode material also provides the basis of expanding the library of suitable anode materials for PIBs.

PIBs are still in the early stages of exploration. To date, the materials that have been evaluated as anode candidates only include: carbonaceous materials (such as graphite, [9-10] hard/soft carbon, [8, 11] heteroatom-doped graphene, [12]) tin-based composites, [13] and phosphorus-based alloys.

1. Introduction

Lithium-ion batteries (LIBs) have achieved tremendous success as a power source for portable electronic devices, electrical vehicles, hybrid electrical vehicles, *etc.* [1] Nevertheless, the scarcity and high cost of lithium reserves demand for the development of alternative energy storage devices. Sodium-ion batteries (SIBs) and potassium ion batteries (PIBs) offer great promise, due to their abundant natural resource availability and low cost. [2-7] SIBs are the preferred option because potassium has larger ionic radius than sodium. Potassium ion based graphite intercalation compounds are also highly stable, which make them suitable for energy storage application. [8] Furthermore, the lower standard hydrogen potential (E_0) of potassium (-2.93 V vs. E_0), compared to that of sodium (-2.71 V vs. E_0) indicate higher voltage and higher energy density for PIBs than for SIBs. [9, 10] Therefore, PIBs have the potential to be a low cost battery with high working voltage and high energy density.

[14] Therefore, it is critical to expand the scope of research on anode materials. To this end, transition metal sulfides with high capacity and enhanced electrical conductivity show promising performance, [15-24] however, the long term stability is still poor. The potential approach to alleviate the poor cycling performance is by hybridisation of active carbon materials with nanostructured quantum dots (QDs). QDs are zero-dimensional materials that have diameter less than 10 nm, large surface area, and short ion/electron transfer path. However, QDs are unstable and vulnerable to self-aggregation when compared to their bulk counterparts. [25] This aggregation could be prevented by controlling the growth of QDs onto a platform. [26] Graphene has a high surface area and could act as an ideal substrate for controlling the growth of QDs. This is because the ions of the QDs materials and electrophilic carbon atoms of graphene could form a strong interaction, which inhibits the aggregation and allows the QDs anchored on graphene nanosheets tightly. [27-28] Therefore, the hybridization of QDs and graphene provide an excellent approach to overcome the challenges on aggregation.

Cobalt sulfide (CoS) has demonstrated applications in supercapacitors, dye-sensitized solar cells, catalysis, LIBs and SIBs. [29] Herein, we investigated novel CoS and graphene hybrids as anode materials for PIBs. These hybrids consist of 10 to 20 nm CoS nanoclusters that are attached on graphene. We used a two-step hydrothermal strategy to achieve the hybrids of CoS and graphene (loading of 25% graphene by mass, referred to as CoS@G-25), which features interconnected CoS nanoclusters uniformly anchored on the graphene sheets. We specifically evaluated the performance of these novel hybrids as anode materials for PIBs at high charge-discharge rates.

H. Gao, T. Zhou, Y. Zheng, Q. Zhang,
Prof. H. Liu, Prof. Z. Guo
Institute for Superconducting and Electronic Materials,
School of Mechanical, Materials and Mechatronics
Engineering,
University of Wollongong,
North Wollongong, NSW 2500, Australia
E-mail: zguo@uow.edu.au

Y Liu, Prof. J. Chen
ARC Centre of Excellence for Electromaterials Science,
Intelligent Polymer Research Institute,
Australian Institute of Innovative Materials,
University of Wollongong,
North Wollongong, NSW 2522, Australia
E-mail: junc@uow.edu.au

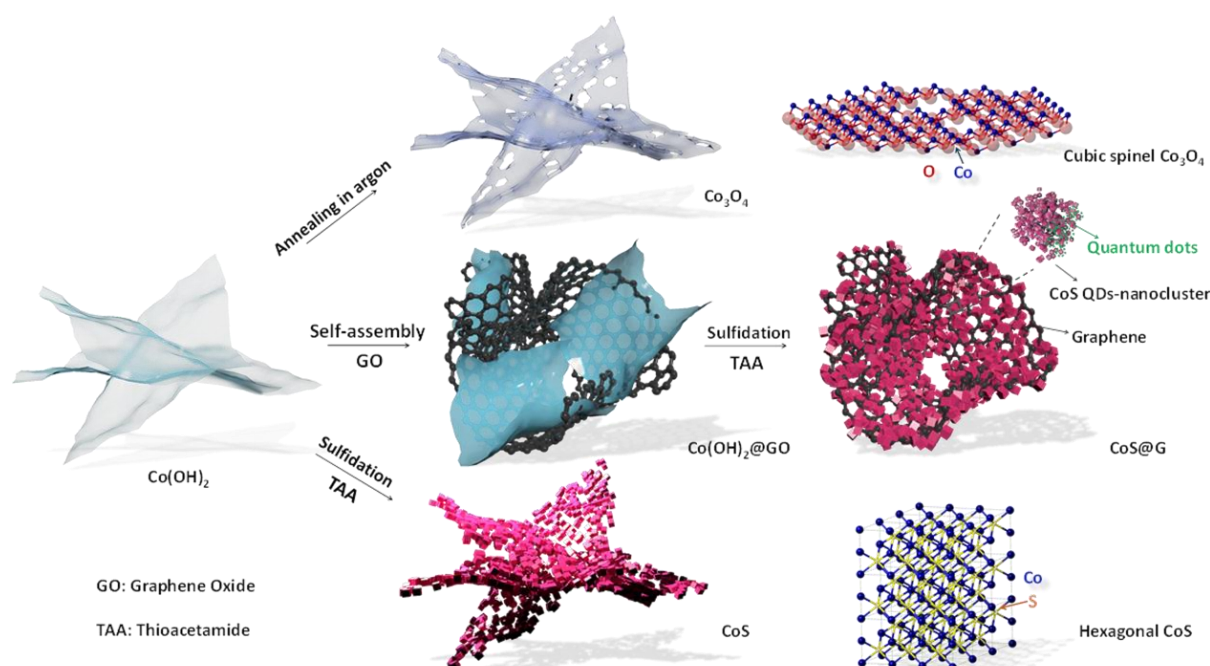
The *in situ* growth of CoS QDs-nanoclusters on graphene endows the hybrid materials with robust and stable interfacial connection between CoS and graphene, which provide structural stability during the charge-discharge process. These hybrids also possess large surface area, effective ion and electron transfer paths, and a highly conductive network. These desirable characteristics are integrated into the composite for superior electrochemical performance and stable long term cycling. Upon testing as PIBs, an unprecedented reversible capacity of 434.5 mA h g⁻¹, and cycle life of 310.8 mA h g⁻¹ after 100 cycles at 500 mA g⁻¹ is obtained. The capacities of 278.3 and 232.3 mA h g⁻¹ at high rates of 3 C and 4 C, respectively, are maintained. To date, this performance is the best among the reported anode materials for PIBs. Furthermore, at high current densities of 3 C and 4 C, the capacity retentions of 67.3% and 56.2% of the capacity at 0.5 C, respectively, is obtained. This performance is superior than SIBs which is only compared to only 51 % and 42.6 %, respectively. This difference highlights that higher potassium ion diffusion than for the sodium ions achieved in the novel hybrid material.

2. Results and Discussion

Scheme 1 shows the fabrication process for CoS@G-25 composite. For comparison, the synthesis processes for pristine CoS and Co₃O₄ are also presented. The two-step hydrothermal strategy includes the following procedures: (i) preparation of 2D cobalt hydroxide (Co(OH)₂) nanosheets; and (ii) *in-situ* sulfidation in the presence of graphene oxide (GO). The pristine CoS was fabricated

under identical conditions, and the Co₃O₄ was obtained *via* annealing the Co(OH)₂ precursor in argon atmosphere. During the sulfidation step, the Co(OH)₂ nanosheets ruptured into CoS nanoclusters. The pristine CoS nanoclusters were 50 to 100 nm in size, which aggregated into micro-sized sheet structure. The CoS nanoclusters in CoS@G-25 composite were only 10 to 20 nm in size, and homogenously distributed on graphene nanosheets. Interestingly, we further detected that every CoS nanocluster with 10 to 20 nm in size is built up from QDs, which interconnected with each other as well. This is mainly because the presence of the graphene, which kindly prevent the aggregation of the nanoclusters. It is well known that the morphology of a material is highly dependent on the intrinsic crystal structure. Here, we present the crystal structures of the as-prepared cubic spinel Co₃O₄ and the hexagonal CoS. For cubic spinel Co₃O₄, the decrease in the long-range order in the third dimension induces the formation of nanosheet structure. As for the hexagonal CoS, the sulfur sublattice packed in the hexagonal structure leads to more significant morphology change of the nanosheets during the sulfidation process. In this work, we investigated the effect of graphene ratio in the composites and obtained CoS@G-10 (with 10% GO) and CoS@G-15 (with 15% GO) in order to optimize the content of graphene in the composite. We also prepared Co₃O₄ on graphene composite (Co₃O₄@G) using the same precursor, and compare their electrochemical properties with those of CoS@G.

Figure. 1a shows the X-ray diffraction (XRD) patterns of CoS@G-25 and CoS. The dominant diffraction peaks of both CoS@G-25 and CoS can be indexed to hexagonal



Scheme 1. Schematic illustration of the synthesis process for CoS@G-25 composite in two steps: (i) the preparation of 2D Co(OH)₂ nanosheets; (ii) in-situ sulfidation with the presence of GO to yield the CoS@G-25. The fabrication processes for Co₃O₄ and pristine CoS are presented as well.

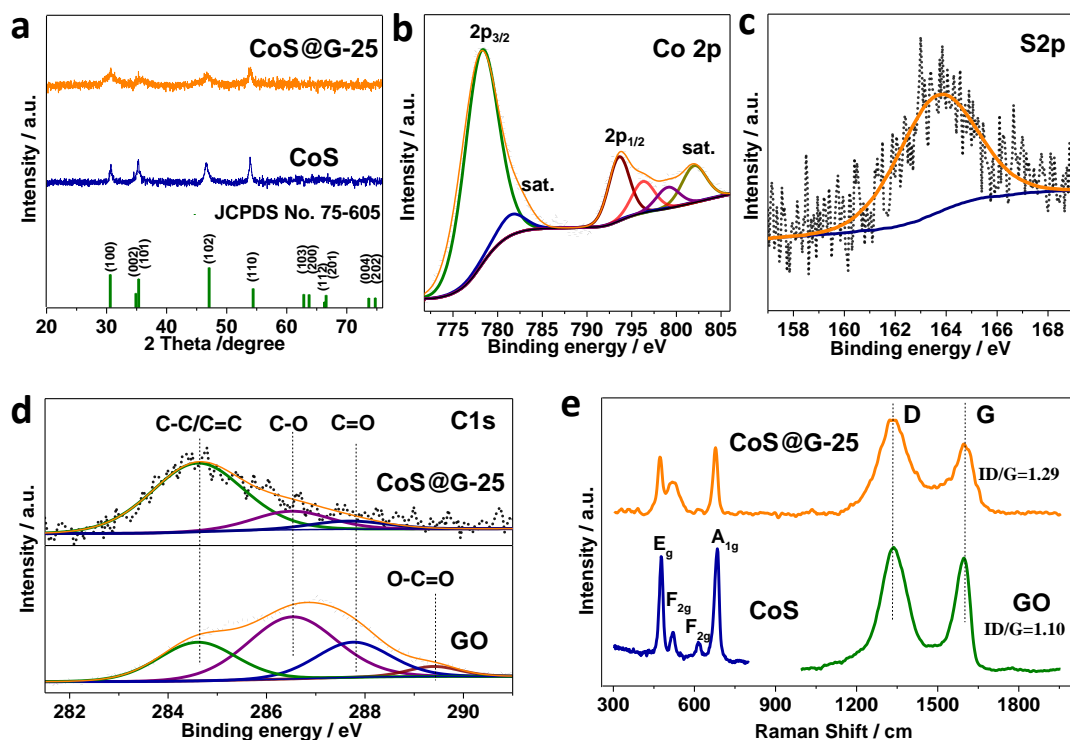


Figure 1. a) XRD patterns of CoS and CoS@G-25; XPS analysis of CoS@G-25: b) Co 2p, c) S 2p, d) C 1s; e) Raman spectra of CoS, GO, and CoS@G-25.

CoS (JCPDS no. 75-605), the same with CoS@G-10 and CoS@G-15 (Figure S1, Supporting information). The graphene contents for CoS@G-10, CoS@G-15, and CoS@G-25 are estimated to be 9.49%, 14.32%, and 24.94%, respectively, according to the thermogravimetric (TG) analysis (Figure S2). Note that the signals of CoS in CoS@G-25 exhibit broader diffraction peaks than the pristine CoS, implying the existence of very tiny particles in CoS@G-25. Figure S3 presents the XRD patterns of Co(OH)_2 and Co_3O_4 . The X-ray photoelectron spectroscopy (XPS) analysis in Figure 1b-d was further used to examine chemical states of cobalt, sulfur, and carbon in the CoS@G-25 composite. Figure 1b gives the Co 2p XPS spectrum of the CoS@G-25 composite. The Co $2p_{3/2}$ spectrum has peaks at 778.0 and 781.6 eV, which can be attributed to Co-S and Co-O bonds, respectively. The Co-O bonds are derived from the coordination between the unstable surface cobalt ions and oxygen atoms from the graphene.^[30-31] The peaks between 791.0 and 806.0 eV are the Co $2p_{1/2}$ signals corresponding to their Co $2p_{3/2}$ counterparts and the satellite signal. The S 2p peak observed at 163.5 eV in Figure 1c exhibits the binding energy of Co-S.^[32] The C 1s XPS spectra of GO and CoS@G-25 are presented in Figure 1d. The spectra of the pure GO can be fitted into four different spectral peaks: a strong peak for carbon in C-O bonds (286.5 eV), along with weaker functional groups, non-oxygenated carbon (C=C, 284.7 eV), carbonyl carbon (C=O, 287.7 eV), and carboxylate carbon (O-C=O, 289.4 eV).^[33-34] In contrast to pure GO, the peak intensity of the

non-oxygenated carbon in CoS@G-25 composite shows a significant increase, and the peak intensity of C-O, C=O and O-C=O bonds exhibit a sharp decrease. It is indicating that GO experiences a sufficient reduction to rGO during the hydrothermal reactions. We further conducted Raman measurements for GO, CoS, and CoS@G-25 composite (Figure 1e). It is obvious that both CoS and CoS@G-25 exhibit Raman peaks at 470, 516, 618 and 675 cm^{-1} , which are assigned to the E_g , F_{2g} , F_{2g} and A_{1g} modes.^[35] In addition, two obvious carbon bands, the D band and G band peaks, could be observed for the CoS@G-25 composite and pure GO, respectively. The D/G intensity ratio of CoS@G-25 composite (1.29) is higher than that of the pure GO (1.10), indicating the reduction of GO to graphene in the composite, which is in agreement with the previous XPS analysis. The N_2 adsorption-desorption isotherms of the CoS@G-25 and CoS are shown in Figure S4.

Figure 2a-c exhibits scanning electron microscope (SEM), bright field, and dark field images of the pristine CoS. The pristine CoS with a micro-sized sheet structure, is built up from medium sized nanoclusters (50-100 nm). The corresponding EDS elemental mapping analysis demonstrates the presence of Co and S elements. (Figure 2d, e and Figure S5) The SEM and transmission electron microscope (TEM) images of the CoS@G-25 composite are shown in Figure 2f-h. It is obvious that there are smaller CoS nanoclusters (10 to 20 nm) in CoS@G-25 composite than in the pristine CoS homogeneously

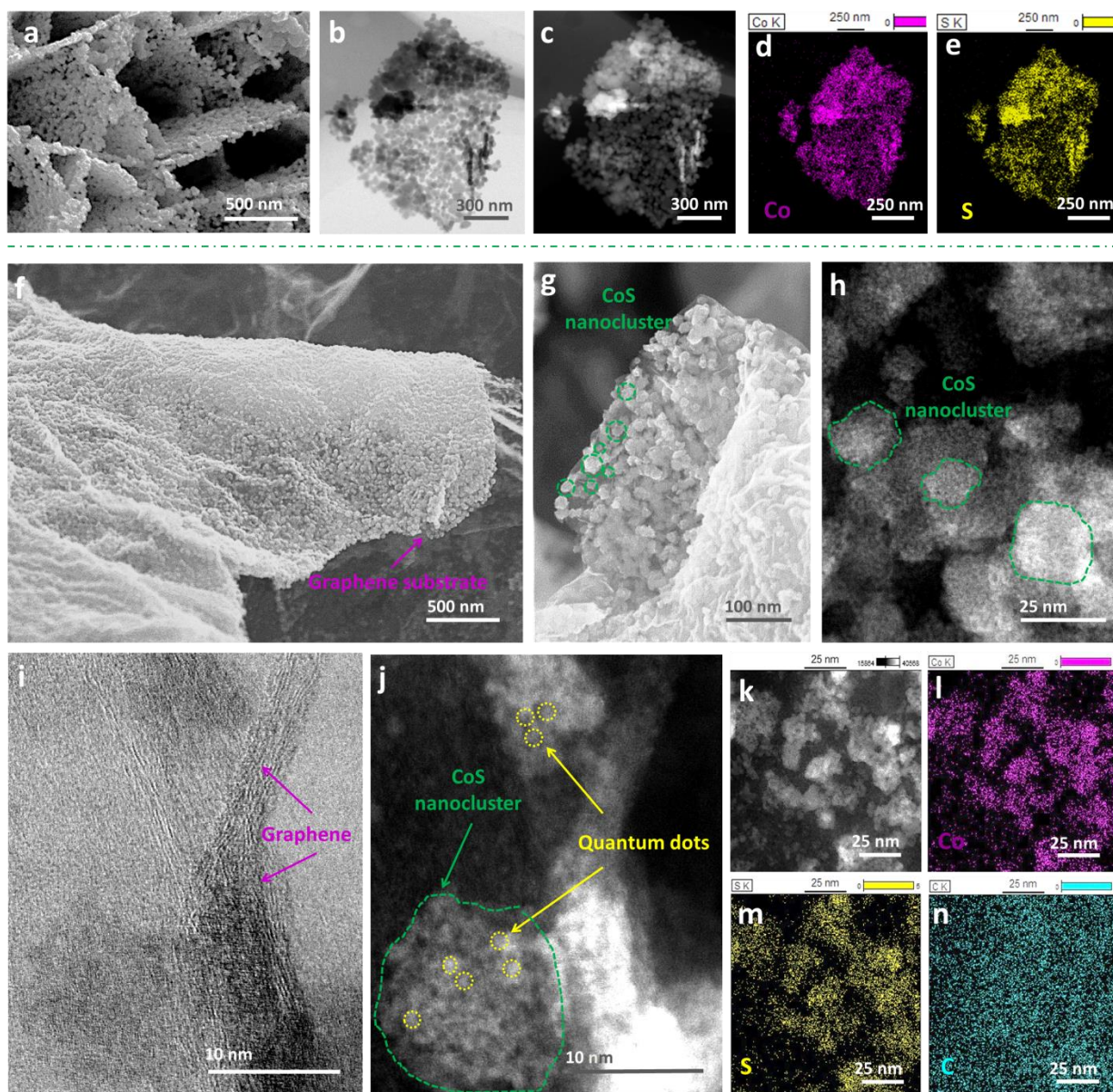


Figure 2. a) SEM, b) bright field, and c) dark field images of CoS; elemental mapping images of: d) cobalt, e) sulfur; f, g) SEM, h) TEM, i) bright field, and j) dark field images of CoS@G-25; k) STEM image and elemental mapping analysis of CoS@G-25: l) cobalt, m) sulfur, and n) carbon.

adhered to the graphene nanosheets. Figure S6 display an SEM image of Co(OH)_2 nanosheets. During the sulfidation process, the CoS nanoclusters nucleate *in situ* and are deposited on the graphene substrate due to the pre-intercalation between the 2D Co(OH)_2 nanosheets and the GO nanosheets. The robust interfacial connection would guarantee the structure stability of the composite. At the same time, the Co(OH)_2 nanosheets raptured into the interlinked CoS nanoclusters with the graphene nanosheets restraining the further growth and controlling the size of the CoS nanoclusters.^[36] In CoS@G-10 composite, most of CoS nanoclusters have aggregated on the graphene nanosheets. Compare to CoS@G-10, the CoS nanoclusters in CoS@G-15 distributed relatively uniform, but still exist aggregation problems. (Figure S7a,

b) This aggregation is mainly because of the excess of CoS. From the bright field and dark field high-resolution TEM images of CoS@G-25 composite in Figure 2i, j, we found that every CoS nanocluster (10 to 20 nm in size) is built up from interconnected QDs. Due to the high surface area and ample active sites represented by the QDs, effective promotion of electron and ion transfer during the electrochemical cycling process could be anticipated. The corresponding scanning TEM (STEM) and EDS elemental mapping analysis of the CoS@G-25 confirms the coexistence and homogenous distribution of Co, S, and C elements in the selected area (Figure 2 k-n and Figure S8). The SEM images of the Co_3O_4 , Co(OH)_2 @G, and Co_3O_4 @G composites and TEM image of Co(OH)_2 @G

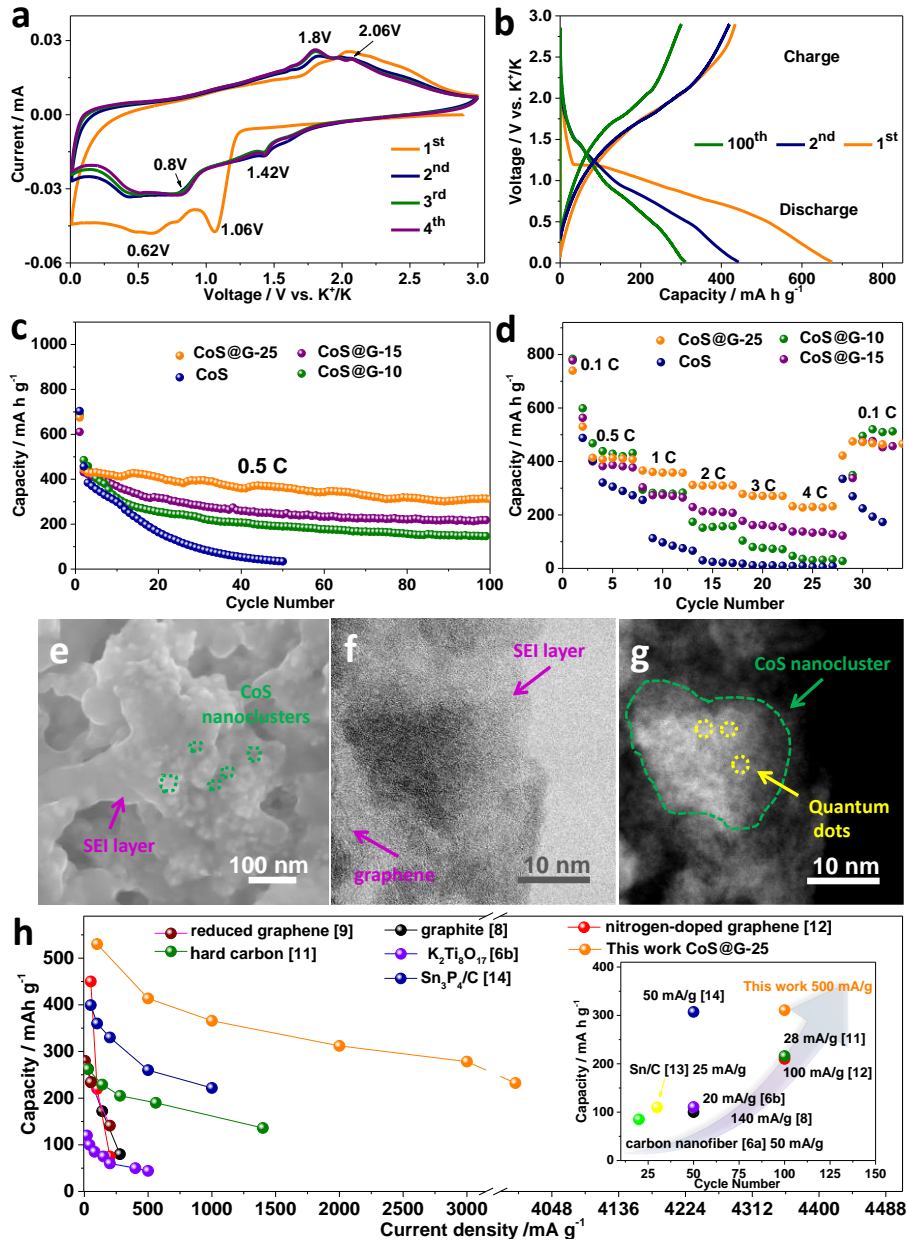


Figure 3. Electrochemical performance of CoS@G-25 electrode for PIBs: a) Cyclic voltammograms (CV) for the first 4 cycles of CoS@G-25; b) Charge-discharge voltage profiles for selected cycles of CoS@G-25 composite at a current density of 0.5 C; c) Cycling and d) Rate performance of CoS, CoS@G-25, CoS@G-10, and CoS@G-15 electrodes; e) SEM, f) bright field, and d) dark field images of CoS@G-25 electrode after 100 cycles; h) Comparison of the rate and cycling (inset) capabilities of the previously reported anode materials for PIBs with our work (1C = 1000 mA g⁻¹).

are shown in Figure S9. The pristine Co₃O₄ features 2D nanosheets with numerous geometrical holes. The layer-by-layer Co(OH)₂@G was the precursor for Co₃O₄@G with solid nanoparticles formed into nanosheets in combination with the graphene.

The electrochemical performance of CoS@G-25 was tested in PIBs and in SIBs for comparison. The cyclic voltammetry (CV) curves for SIBs are presented in Figure S10a. A peak at ~0.9 V in the first sweeping cycle may belong to the initial insertion of sodium, the following peak at ~0.6 V appeared and decreased in the following

negative scans, which correspond to the formation of solid-electrolyte interphase (SEI) film. Afterwards, the reduction peaks in the following scans attributed to the insertion of sodium, and the conversion reaction to form Na₂S and Co. [18] Figure 3a shows the CV curves of CoS@G-25 electrode for PIBs. A peak at ~1.06 V in the first cathodic scan should attribute to the insertion of potassium, and the peak at ~0.62 V should be the SEI film formation. [29] After the first scan, the reduction/oxidation peaks in the following scans are almost the same as in SIBs,

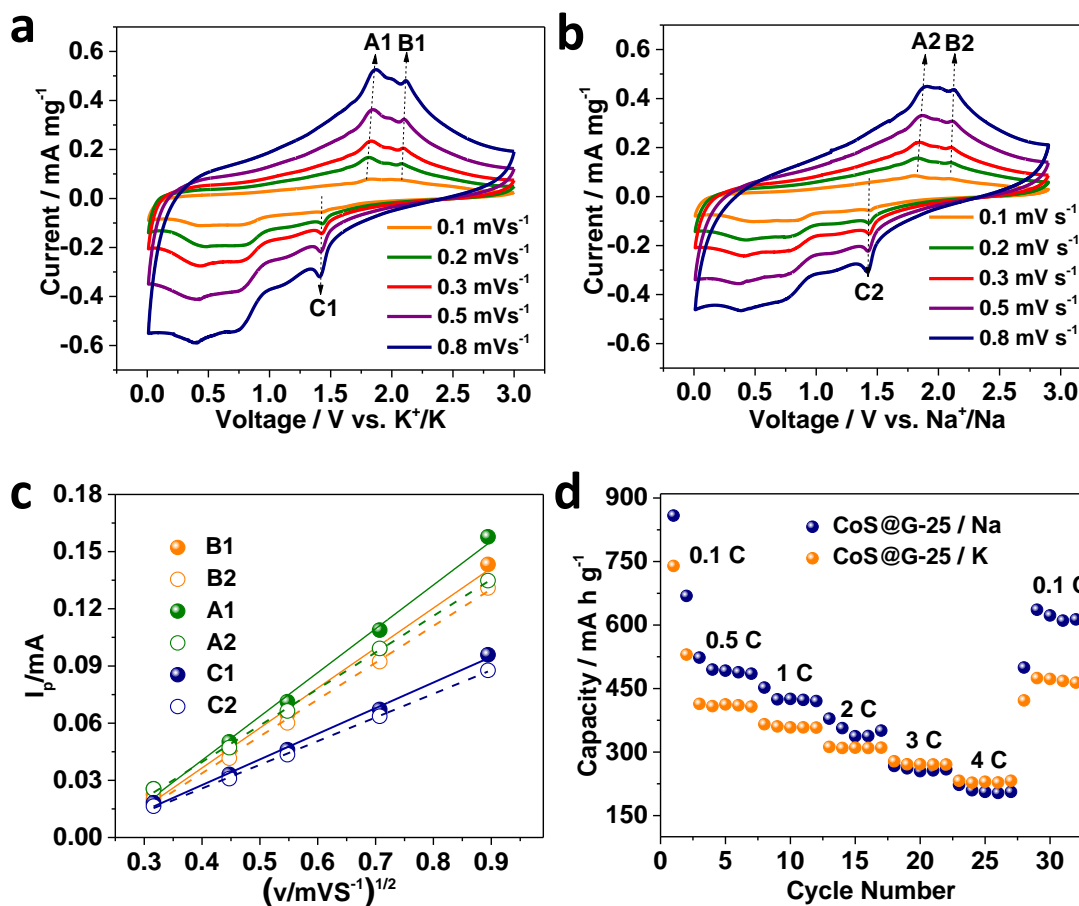


Figure 4. CV curves of CoS@G-25 electrode at different scan rates: a) PIBs and b) SIBs; c) linear relationship of peak currents versus $V^{0.5} s^{-0.5}$ and the corresponding linear fits; d) comparison of rate performance for the CoS@G-25 electrode in SIBs and PIBs at different current densities.

demonstrating the similar electrochemical mechanism to SIBs. It is worth noting that all the redox peaks in the CV curves for both SIBs and PIBs are well matched to the sodiation-desodiation plateaus and potassiation-depotassiation plateaus, respectively (Figure S10b and Figure 3b). Figure 3c displays the cycling performance of CoS@G-25, CoS@G-10, CoS@G-15 and CoS electrodes at a current density of 0.5 C within the voltage range of 0.01 to 2.9 V for PIBs. Dramatic capacity fading can be obviously detected from the CoS electrode curve, while relatively stable cycling performances are observed from the CoS@G-10 and CoS@G-15 electrodes. The CoS@G-25 electrode, however, displays a more stable cycle life than those of the CoS@G-10 and CoS@G-15 electrodes. The CoS@G-25 electrode reveals good cycling stability from the second cycle onward, delivering an initial capacity of 675.0 mA h g⁻¹ with initial coulombic efficiency of 64.4% (Figure S12a) and a discharge capacity of 310.8 mA h g⁻¹ in the 100th cycle, delivering ~ 70.2 % of the second cycle capacity. In case of the SIBs in Figure S10c, the CoS@G-25 electrode exhibits the best cycling performance as well. It delivers initial discharge/charge capacities of 799.3/547.9 mA h g⁻¹ with initial coulombic efficiency of ~ 68.6% (Figure S12b), with the discharge capacity

gradually decreasing to 438.4 mA h g⁻¹ after 100 cycles with a capacity retention of ~ 80.0 %. The capacity of pristine CoS electrode drops quickly after ~40 cycles. Figure S11 shows the SEM images of the electrode and digital photos of the separator after the 10th cycle and the 50th cycle.

The rate capabilities for both PIBs and SIBs were also compared. (Figure 3d and Figure S10d) The CoS@G-25 electrode clearly shows the best rate capability in both PIBs and SIBs. Figure S13 shows the electrochemical impedance spectroscopy (EIS) results of CoS@G-25 electrode for SIBs and PIBs, respectively. The high frequency semicircles of the CoS@G-25 composite in both SIBs and PIBs remain low value after 40 cycles, indicating fast Na/K ions reaction between CoS QDs-clusters and high electron transport rate during the cycle life. For comparison, the electrochemical performances of the Co₃O₄ and Co₃O₄@G electrodes in SIBs and PIBs are presented in Figure S14. Obviously, the capacities of both the Co₃O₄ and the Co₃O₄@G electrodes are lower than those of the CoS and CoS@G electrodes in both SIBs and PIBs. This demonstrates that the metal sulfides behave higher capacities than that of their oxide counterpart. The cycling performance of graphene for PIBs and SIBs are

also investigated. (Figure S15). Figure S16 shows the SEM image, TGA and cycling performance of the CoS@G-35 composite.

Figure 3e-g shows SEM, bright field, and dark field images of CoS@G-25 electrode after 100 cycles at 500 mA g⁻¹ for PIBs. It is clear that the CoS nanoclusters with 10-20 nm in size remain anchored on the graphene nanosheets. The bright field and dark field images demonstrate the existence of the QDs after cycling, indicating the superior structural stability of the electrode. The SEM image of fresh CoS@G-25 electrode is displayed in Figure S17. Figure 3h compares the rate capabilities and cycling performances (inset diagram) of the previously reported anode materials for PIBs with our work. Obviously, our work presents the best electrochemical performance among all the reported anode materials.

We investigated the CV curves for CoS@G-25 electrode at different scan rates from 0.1 to 0.8 mV s⁻¹ for both SIBs and PIBs (marked as CV/Na and CV/K, respectively) in Figure 4a, b. The intensities of both cathodic and anodic peaks in the CV/Na and CV/K curves vary with the scan rate. The scan rate increases from 0.1 to 0.8 mV s⁻¹, and both the CV/K and CV/Na curves preserve their basic CV profiles, indicating a fast response capability to the quick scan rate for both SIBs and PIBs. It is well known that the charge/discharge reaction rate is diffusion-controlled.^[37]

The Na⁺/K⁺ diffusion coefficient (D_{Na^+/K^+}) can be calculated based on the Randles-Sevcik equation (Eq.(1)). (Note: i_p , n , and F represent peak current, number of electrons, and the Faraday constant, respectively. D , R , and T are the diffusion coefficient, gas constant, and temperature, respectively. A , C , and v stands for the surface area of electrode, concentration of Sodium/potassium ions, and voltage scanning rate, respectively). Since the CoS@G-25 electrode was prepared and tested by the same procedure, the Na⁺/K⁺ diffusion coefficient (D_{Na^+/K^+}) can be calculated based on the simplified Randles-Sevcik equation (Eq.(2)).^[38]

$$i_p = 0.4663nF \sqrt{\frac{nFD}{RT}} AC\sqrt{v} \quad (1)$$

$$i_p = a\sqrt{D}\sqrt{v} \quad (2)$$

where a is supposed to be constant for the cells applied in sodium/potassium ion batteries, and $aD^{1/2}$ is defined as the apparent diffusion coefficient of Na⁺/K⁺ in the cells. The linear relationship between the peak currents (i_p : A1/A2, B1/B2, C1/C2) and the square root of the scan rate ($v^{1/2}$) is presented in Figure 4c. Obviously, the peak currents exhibit a linear relationship with $v^{1/2}$, and the electrode applied in PIBs shows a higher diffusion coefficient than in SIBs, indicating a better rate performance of CoS@G-25 electrode in PIBs than in SIBs. In order to confirm this deduction, Figure 4d intuitively

compares the rate capability of the CoS@G-25 electrode in SIBs and PIBs. Apparently, at the high rates of 3 C and 4 C, CoS@G-25 in PIBs shows better capability than in the SIBs. In PIBs, 67.3 % and 56.2 % of the electrode's capacity are retained at 0.5 C, respectively, while only 51% and 42.6% of capacity are retained for SIBs.

3. Conclusion

In summary, the CoS QDs-nanoclusters uniformly anchored on graphene nanosheets have been fabricated via a facile two-step hydrothermal strategy. The coexistence of CoS QDs-nanoclusters and graphene nanosheets endow the composite with a large surface area and a highly conductive network. In addition, the strong interfacial connections between graphene and CoS can guarantee robust structural stability that can tolerate insertion-deinsertion of ions in the electrochemical cycling process. Therefore, a superior electrochemical energy performance could be anticipated. We initially applied CoS@G-25 for PIBs, and the as-prepared CoS@G-25 electrode delivered an incredible capacity of 310.8 mA h g⁻¹ after 100 cycles at 500 mA g⁻¹. What is more, compared to the behaviour in SIBs, the CoS@G-25 electrode exhibits better high rate performance in PIBs, indicating the high energy storage potential of the CoS@G-25 electrode in PIBs. All of the results indicate that PIBs are a better alternative choice at high charge-discharge rates compared to the SIBs. In addition, the CoS@G-25 as a new candidate would help to broaden the data-base of potential suitable anode materials for PIBs.

4. Experimental Section

Preparation of Co(OH)₂ nanosheet precursor: In a typical procedure, deionised water and ethylene glycol in a volume ratio of 1: 1.5 were mixed together to obtain solution A. Co(NO₃)₂·6H₂O and hexamethylene tetramine in a molar ratio of 1: 2 were dissolved in the solution under vigorous stirring. Then the resultant pink solution was transferred to a Teflon-lined stainless-steel autoclave and heated to 130 °C for 6 h. The product was washed with anhydrous ethanol and deionized (DI) water several times before drying at 60 °C overnight.

Synthesis of CoS@G-25, CoS@G-10, CoS@G-15 and CoS: Graphene oxide (GO) was synthesized by Hummers' method. The progress of the synthesis of CoS@G-25 composite is illustrated in Scheme 1. The above Co(OH)₂ precursor (30 mg) was redispersed into ethanol (30 mL), and the as-prepared graphene oxide dispersed in ethanol (GO, 4.0 mg mL⁻¹, 5 mL) was added into the solution. After magnetic stirring for 30 mins, thioacetamide (TAA, 50 mg) was dissolved into the mixture. Then, the mixture was transferred into a Teflon-lined stainless steel autoclave and kept at 160 °C for 3 h. After cooling to room temperature, the sample was collected by centrifugation at the speed of 400 rpm for 2mins, washed with ethanol

2-3 times, and then dried in a vacuum oven at 60 °C overnight. For comparison, CoS@G-10 (with 10 percent GO) and CoS@G-15 (with 15 percent GO) composites and pure CoS without the presence of GO were also prepared by the above procedure.

Synthesis of Co₃O₄@G and Co₃O₄ Composites: In a typical batch, the above Co(OH)₂ precursor (30 mg) was redispersed into ethanol (30 mL), and the as-prepared graphene oxide (GO, 4.0 mg mL⁻¹, 2 mL) was added into the solution. After magnetic stirring for 30 min, the mixture was transferred into a Teflon-lined stainless steel autoclave and kept at 160 °C for 3 h. After cooling to room temperature, the sample was collected by centrifugation, washed with ethanol several times, and then dried in a vacuum oven at 60 °C overnight. The as-prepared product was then annealed with a ramp rate of 5 °C/min to 450 °C for 5 h in flowing argon atmosphere. For comparison, pure Co₃O₄ composite was also prepared by annealing the Co(OH)₂ precursor in flowing argon with a ramp rate of 5 °C/min to 450 °C for 5 h.

Characterization: The structures of the as-prepared materials were characterized by X-ray diffraction, which was conducted on a GBC MMA XRD ($\lambda = 1.54 \text{ \AA}$) with the voltage kept at -40 kV and current kept at 25 mA. Raman spectra were collected on a JOBIN Yvon Horiba Raman spectrometer model HR800, using a 10 mW helium/neon laser at 632.8 nm excitation. X-ray photoelectron spectroscopy (XPS) was carried out on a VG Multilab 2000.

Thermogravimetric analysis (TGA) measurements were conducted in argon at the rate of 10 °C min⁻¹ using a Mettler Toledo TGA/DSC1. The morphologies and particle sizes of the samples were investigated by field emission scanning electron microscopy (JEOL JSM-7500FA) and transmission electron microscopy (JEOL 2011, 200 keV). The TEM was linked to an energy dispersive spectral analysis (EDS) system, which used a probe corrected JEOL ARM200F. N₂ adsorption-desorption isotherms were obtained by using a Micromeritics Tristar II analyzer at the testing temperature of 77 K. The Brunauer-Emmett-Teller (BET) surface area was calculated using experimental points at a relative pressure of $P/P_0 = 0.05-0.25$. The pore size distribution was derived from the adsorption branch using the Barrett-Joyner-Halenda (BJH) method. The total pore volume was estimated the amount of nitrogen adsorbed at a relative pressure (P/P_0) of 0.995.

Electrochemical measurements: For the electrochemical measurements of CoS@G-25, CoS@G-10, CoS@G-15, CoS, Co₃O₄@G and Co₃O₄ as anode materials, CR2032 coin type cells were prepared. The electrodes were prepared by mixing the CoS@G-25, CoS@G-10, CoS@G-15, CoS, Co₃O₄@G and Co₃O₄ with sodium carboxymethyl cellulose and Super P in a weight ratio of 8:1:1, respectively. The resultant slurries were coated on copper foil and dried in a vacuum oven at 80 °C overnight, followed by pressing at 30 MPa. Na/K foil was used as

both counter and reference electrode, and the separator was glass microfiber (Whatman). The electrolyte for SIBs was NaClO₄ (1.0 mol L⁻¹) in an ethylene carbonate (EC) / diethyl carbonate (DEC) solution (1:1 v/v), while for PIBs, it was KPF₆ (0.6 mol L⁻¹) in an ethylene carbonate (EC) / diethyl carbonate (DEC) solution (1:1 v/v). All the cells were assembled in a glove box under argon atmosphere, using a Land Battery-Testing System at room temperature.

Supporting Information

Supporting Information is available from the Wiley Online Library or from the author.

Acknowledgments

Support from the Australian Research Council (ARC) through an ARC Discovery project (DP170102406), (DP170102320) and Future Fellowship (FT150100109) are gratefully acknowledged. The authors would also like to thank the Australian National Fabrication Facility (ANFF) for equipment access, the Electron Microscopy Centre (EMC) at the University of Wollongong for the electron microscopy characterizations, and Dr. Tania Silver for critical reading of the manuscript and valuable remarks.

Received: ((will be filled in by the editorial staff))

Revised: ((will be filled in by the editorial staff))

Published online: ((will be filled in by the editorial staff))

-
- [1] a) Y. Zheng, T. Zhou, X. Zhao, W. K. Pang, H. Gao, S. Li, Z. Zhou, H. Liu, Z. Guo, *Adv. Mater.* **2017**, DOI: 10.1002/adma.201700396; b) T. Zhou, Y. Zheng, H. Gao, S. Min, S. Li, H. Liu, Z. Guo, *Adv. Sci.* **2015**, 2, 1500027; c) J. Yang, Y. Wang, W. Li, L. Wang, Y. Fan, W. Jiang, W. Luo, Y. Wang, B. Kong, C. Selomulya, H. Liu, S. Dou, D. Zhao, *Adv. Mater.* **2017**, 1700523; d) W. Liu, T. Zhou, Y. Zheng, J. Liu, C. Feng, Y. Shen, Y. Huang, Z. Guo, *ACS Appl. Mater. Interfaces* **2017**, 9 9778.
 - [2] a) N. Yabuuchi, K. Kubota, M. Dahbi, S. Komaba, *Chem. Rev.* **2014**, 114, 11636; b) C. Chen, H. Xu, T. Zhou, Z. Guo, L. Chen, M. Yan, L. Mai, P. Hu, S. Cheng, Y. Huang, J. Xie, *Adv. Energy Mater.* **2016**, 6, 1600322; c) S. Li, Y. Dong, L. Xu, X. Xu, L. He, L. Mai, *Adv. Mater.* **2014**, 26, 3545.
 - [3] a) H. Ye, L. Wang, S. Deng, X. Zeng, K. Nie, P. Duchesne, B. Wang, S. Liu, J. Zhou, F. Zhao, N. Han, P. Zhang, J. Zhong, X. Sun, Y. Li, Y. Li, J. Lu, *Adv. Energy Mater.* **2017**, 7, 1601602; b) P. Wang, Y. You, Y. Yin, Y. Wang, L. Wan, L. Gu, Y. Guo, *Angew. Chem.* **2016**, 128, 7571; c) C. Fang, Y. Huang, W. Zhang, J. Han, Z. Deng, Y. Cao, H. Yang, *Adv. Energy Mater.* **2016**, 6, 1501727.
 - [4] a) H. Gao, T. Zhou, Y. Zheng, Y. Liu, J. Chen, H. Liu, Z. Guo, *Adv. Energy Mater.* **2016**, 6, 1601037; b) T. Zhou, W. K. Pang, C. Zhang, J. Yang, Z. Chen, H. K. Liu, Z. Guo,

- ACS Nano, **2014**, 8, 8323; c) C. Zhu, X. Mu, P. A. van Aken, Y. Yu, J. Maier, *Angew. Chem.* **2014**, 126, 2184.
- [5] a) C. Wessells, S. Peddada, R. Huggins, Y. Cui, *Nano Lett.* **2011**, 11, 5421; b) D. Su, A. McDonagh, S. Qiao, G. Wang, *Adv. Mater.* **2017**, 29, 1604007.
- [6] a) Y. Liu, F. Fan, J. Wang, Y. Liu, H. Chen, K. L. Jungjohann, Y. Xu, Y. Zhu, D. Bigio, T. Zhu, C. Wang, *Nano Lett.* **2014**, 14, 3445; b) J. Han, M. Xu, Y. Niu, G. Li, M. Wang, Y. Zhang, M. Jia, C. Li, *Chem. Commun.* **2016**, 52, 11274.
- [7] Z. Jian, Y. Liang, I. A. Rodríguez-Pérez, Y. Yao, X. Ji, *Electrochem. Commun.* **2016**, 71, 5.
- [8] Z. Jian, W. Luo, X. Ji, *J. Am. Chem. Soc.* **2015**, 137, 11566.
- [9] W. Luo, J. Wan, B. Ozdemir, W. Bao, Y. Chen, J. Dai, H. Lin, Y. Xu, F. Gu, V. Barone, *Nano Lett.* **2015**, 15, 7671.
- [10] S. Komaba, T. Hasegawa, M. Dahbi, K. Kubota, *Electrochem. Commun.* **2015**, 60, 172.
- [11] Z. Jian, Z. Xing, C. Bommier, Z. Li, X. Ji, *Adv. Energy Mater.* **2016**, 6, 1501874.
- [12] a) K. Share, A. P. Cohn, R. Carter, B. Rogers, C. L. Pint, *ACS Nano*, **2016**, 10, 9738; b) G. Ma, K. Huang, J. Ma, Z. Ju, Z. Xing, Q. Zhuang, *J. Mater. Chem. A*, **2017**, 5, 7854; Z. Ju, S. Zhang, Z. Xing, Q. Zhuang, Y. Qiang, Y. Qian, *ACS Appl. Mater. Interfaces*, **2016**, 8, 20682.
- [13] I. Sultana, T. Ramireddy, M. M. Rahman, Y. Chen, A. M. Glushenkov, *Chem. Commun.* **2016**, 52, 9279.
- [14] W. Zhang, J. Mao, S. Li, Z. Chen, Z. Guo, *J. Am. Chem. Soc.* **2017**, 139, 3316.
- [15] Y. Denis, P. V. Prihodchenko, C. W. Mason, S. K. Batabyal, J. Gun, S. Sladkevich, A. G. Medvedev, O. Lev, *Nat. Commun.* **2013**, 4, 2922.
- [16] Y. Zheng, T. Zhou, C. Zhang, J. Mao, H. Liu, Z. Guo, *Angew. Chem. Int. Ed.* **2016**, 55, 3408.
- [17] Z. Hu, L. Wang, K. Zhang, J. Wang, F. Cheng, Z. Tao, J. Chen, *Angew. Chem.* **2014**, 126, 13008.
- [18] a) J. Xie, S. Liu, G. Cao, T. Zhu, X. Zhao, *Nano Energy* **2013**, 2, 49; b) J. Zhou, Y. Wang, J. Zhang, T. Chen, H. Song, H. Yang, *Nanoscale*. **2016**, 8, 14992; c) Y. Chen, X. Li, K. Park, L. Zhou, H. Huang, Y. Mai, J. Goodenough, *Angew. Chem. Int. Ed.* **2016**, 55, 1.
- [19] Z. Shadike, M. H. Cao, F. Ding, L. Sang, Z.-W. Fu, *Chem. Commun.* **2015**, 51, 10486.
- [20] Y. N. Ko, Y. C. Kang, *Carbon* **2015**, 94, 85.
- [21] X. Rui, H. Tan, Q. Yan, *Nanoscale* **2014**, 6, 9889.
- [22] X. Y. Yu, L. Yu, L. Shen, X. Song, H. Chen, X. W. D. Lou, *Adv. Funct. Mater.* **2014**, 24, 7440.
- [23] R. Wu, D. P. Wang, X. Rui, B. Liu, K. Zhou, A. W. Law, Q. Yan, J. Wei, Z. Chen, *Adv. Mater.* **2015**, 27, 3038.
- [24] S. H. Choi, Y. N. Ko, J. K. Lee, Y. C. Kang, *Adv. Funct. Mater.* **2015**, 25, 1780.
- [25] a) C. Chen, L. Wang, Y. Liu, Z. Chen, D. Pan, Z. Li, Z. Jiao, P. Hu, C.-H. Shek, C. L. Wu, *Langmuir* **2013**, 29, 4111; b) D. Dutta, S. Chandra, A. K. Swain, D. Bahadur, *Anal. Chem.* **2014**, 86, 5914.
- [26] a) M. Y. Ye, Z. H. Zhao, Z. F. Hu, L. Q. Liu, H. M. Ji, Z. R. Shen, T. Y. Ma, *Angew. Chem. Int. Ed.* **2017**, 56, 1; b) J. Yang, L. Xi, J. Tang, F. Chen, L. Wu, X. Zhou, *Electrochimica Acta*. **2016**, 217, 274; c) B. De, J. Balamurugan, N. H. Kim, J. H. Lee, *ACS Appl. Mater. Inter.* **2017**, 9, 2459; d) S. J. Yang, S. Nam, T. Kim, J. H. Im, H. Jung, J. H. Kang, S. Wi, B. Park, C. R. Park, *J. Am. Chem. Soc.* **2013**, 135, 7394; e) R. Wang, M. Han, Q. Zhao, Z. Ren, C. Xu, N. Hu, H. Ning, S. Song, J.-M. Lee, *Electrochim. Acta*. **2017**, 243, 152.
- [27] C. Peng, B. Chen, Y. Qin, S. Yang, C. Li, Y. Zuo, S. Liu, J. Yang, *ACS Nano*. **2012**, 6, 1074.
- [28] E. G. S. Firmiano, M. A. L. Cordeiro, A. C. Rabelo, C. J. Dalmaschio, A. N. Pinheiro, E. C. Pereira, E. R. Leite, *Chem. Commun.* **2012**, 48, 7687.
- [29] a) S. Peng, X. Han, L. Li, Z. Zhu, F. Cheng, M. Srinivansan, S. Adams, S. Ramakrishna, *Small* **2016**, 12, 1359; b) S. Peng, L. Li, X. Han, W. Sun, M. Srinivasan, S. G. Mhaisalkar, F. Cheng, Q. Yan, J. Chen, S. Ramakrishna, *Angew. Chem.* **2014**, 126, 12802; c) P. Sennu, M. Christy, V. Aravindan, Y.-G. Lee, K. S. Nahm, Y.-S. Lee, *Chem. Mater.* **2015**, 27, 5726; d) Y. Wang, J. Wu, Y. Tang, X. Lü, C. Yang, M. Qin, F. Huang, X. Li, X. Zhang, *ACS Appl. Mater. Inter.* **2012**, 4, 4246; e) H. Li, Y. Gao, Y. Shao, Y. Su, X. Wang, *Nano Lett.* **2015**, 15, 6689; f) R. Rakhi, N. A. Alhebshi, D. H. Anjum, H. N. Alshareef, *J. Mater. Chem. A* **2014**, 2, 16190.
- [30] Q. Liu, J. Zhang, *CrystEngComm* **2013**, 15, 5087.
- [31] Q. Wang, L. Jiao, H. Du, Y. Si, Y. Wang, H. Yuan, *J. Mater. Chem.* **2012**, 22, 21387.
- [32] C.-W. Kung, H.-W. Chen, C.-Y. Lin, K.-C. Huang, R. Vittal, K.-C. Ho, *ACS Nano* **2012**, 6, 7016.
- [33] S. Stankovich, D. A. Dikin, R. D. Piner, K. A. Kohlhaas, A. Kleinhammes, Y. Jia, Y. Wu, S. T. Nguyen, R. S. Ruoff, *Carbon* **2007**, 45, 1558.
- [34] H. J. Shin, K. K. Kim, A. Benayad, S. M. Yoon, H. K. Park, I. S. Jung, M. H. Jin, H. K. Jeong, J. M. Kim, J. Y. Choi, *Adv. Funct. Mater.* **2009**, 19, 1987.
- [35] a) C.-Y. Chen, Z.-Y. Shih, Z. Yang, H.-T. Chang, *J. Power Sources* **2012**, 215, 43; b) V. Hadjiev, M. Lliev, I. Vergilov, *J. Phys. C: Solid State Phys.* **1988**, 2, L199.
- [36] B. Luo, Y. Fang, B. Wang, J. Zhou, H. Song, L. Zhi, *Energy. Environ. Sci.* **2012**, 5, 5226.
- [37] W. Sun, X. Rui, D. Yang, Z. Sun, B. Li, W. Zhang, Y. Zong, S. Madhavi, S. Dou, Q. Yu, *ACS Nano* **2015**, 9, 11371.
- [38] a) X. Rui, N. Yesibolati, S. Li, C. Yuan, C. Chen, *Solid State Ionics* **2011**, 187, 58; b) S. Tang, M. Lai, L. Lu, *J. Alloys Compd.* **2008**, 449, 300; c) H. Wang, W. Zhang, H. Liu, Z. Guo, *Angew. Chem. Int. Ed.* **2016**, 55, 3992; d) C. Laoire, S. Mukerjee, K. Abraham, *J. Phys. Chem. C*, **2009**, 113, 20127.

